Advanced Energy Materials

ADVANCED ENERGY MATERIALS
www.advenergymat.de

RESEARCH ARTICLE

A New Route to High-Performance Halide-Based Solid-State Batteries: Perfluoropolyether Enables Ion Transport Expansion and Interfacial Protection

Qing Huang[1,2] | Mingtan Wang[2] | Hongming Yi[2] | Kangjun Lu[2] | Peilin Liang[3] | Miao Zhang[2] | Shuaishuai Zhang[2] | Dengyue Ji[2] | Pengyu Chen[2] | Xing Dai[4] | Bingqing Xu[5] | Zheng Li[1,2] | Chuanjin Tian[1] | Linfeng Hu[3] | Xue Zhang[2]

[1]School of Materials Science and Engineering, Jingdezhen Ceramic University, Jingdezhen, P. R. China | [2]Qingtao (KunShan) Energy Development Group Co., Ltd., Kunshan, P. R. China | [3]School of Materials Science and Engineering, Southeast University, Nanjing, P. R. China | [4]State Key Laboratory of Radiation Medicine and Protection, Soochow University, Suzhou, P. R. China | [5]School of Chemistry and Chemical Engineering, Nanjing University of Science and Technology Nanjing, Jiangsu, P. R. China

Correspondence: Zheng Li (lizheng@jsqingtao.com) | Chuanjin Tian (tianchuanjin@jcu.edu.cn) | Linfeng Hu (linfenghu@seu.edu.cn) | Xue Zhang (zhangxue@qingtao.pro)

Received: 17 March 2026 | **Revised:** 17 March 2026 | **Accepted:** 8 April 2026

Keywords: cathode electrolyte interphase | film-forming additives | halide solid-state electrolytes | solid-state batteries

ABSTRACT

Halide-based solid-state batteries (SSBs) promise high energy density and inherent safety but are constrained by sluggish Li^+ transport and interfacial instabilities in composite cathodes. Filling voids with fluid organic could provide a compliant interface contact. Yet, halide SSEs are highly reactive with organics. Here, we systematically assess the chemical compatibility of functional organic molecules with halide SSEs and identify perfluoropolyether (PFE) as an exceptionally stable functional organic toward the cost-effective halide SSEs $Li_{1.75}ZrCl_{4.75}O_{0.5}$ (LZCO). Owing to its low volatility, high wettability, and intrinsic nonflammability, PFE is readily integrated into composite cathodes via dry-electrode processing without compromising the safety of SSBs. During cycling, PFE scavenges deintercalated Li^+ and forms an in situ fluoropolyether-LiF hybrid cathode electrolyte interphase (CEI). This conformal CEI converts discrete point contacts between $LiNi_{0.82}Co_{0.14}Mn_{0.04}O_2$ (Ni82) and LZCO into continuous areal contacts. Rapid Li^+ transport through the highly conductive CEI reactivates the previously isolated Ni82 particles. Concurrently, the robust CEI suppresses parasitic reactions including electrolyte oxidation, O_2 evolution, rock-salt phase formation, Li/Ni mixing, and particle cracking of Ni82. Cathodes containing PFE deliver 206 mAh g^{-1} at 0.1C and exhibit 83% capacity retention after 1500 cycles at 0.5C. Pouch-cell validation underscores the scalability of PFE for commercially viable SSBs.

1 | Introduction

Solid-state batteries (SSBs) have drawn intense interest from academia and industry for their high energy density and inherent safety [1, 2]. Among solid-state electrolytes (SSEs), sulfide and halide chemistries are especially attractive: their relatively low Young's moduli permit densification by cold pressing, and their high room-temperature Li^+ conductivities support excellent electrochemical performance in batteries [3, 4]. In practice, relative to sulfide SSEs, halide SSEs typically exhibit higher oxidative stability and wider safety margins, making them attractive for use in composite cathodes [5–7]. Among halide SSEs, $Li_{1.75}ZrCl_{4.75}O_{0.5}$ (LZCO) has demonstrated advantages in room-temperature ionic conductivity, compressibility, and cost-effectiveness, which are

considered prerequisites for the prospective commercialization of SSBs [8–10].

Despite these advantages, the practical deployment of halide SSEs in composite cathodes remains constrained by cathode-electrolyte interfacial incompatibility [11, 12]. The dominant challenges include: (i) substantial interfacial resistance resulting from rigid, nonconformal contact between SSEs and cathode materials [13]; (ii) mechanical degradation of ion conduction pathways due to anisotropic volumetric expansion and contraction of cathode particles during cycling [14, 15]; and (iii) electrochemical and chemical instability at the interphase between SSEs and cathode materials, leading to a progressive increase in interfacial impedance [16, 17].

To facilitate ionic transport within composite electrodes and improve interfacial stability, two primary strategies have been pursued: material innovation and structural engineering. Cathode surface coatings (e.g., $LiNbO_3$) have proven effective in suppressing parasitic reactions at cathode-halide SSEs interfaces [18]. In parallel, doping strategies, such as the incorporation of F or Ta into Li_3InCl_6, have expanded the electrochemical stability window from 4.20 to 5.13 V while preserving a low Li^+-migration barrier [19, 20]. Furthermore, structural optimization of composite cathodes through a cathode-homogenization strategy and particle-size tailoring has strengthened the ion-transport network in composite cathodes, thereby yielding improvements in electrochemical performance [21, 22].

In sulfide systems, organic-molecule-mediated interfacial regulation has proven effective for enhancing solid-solid contact [23, 24]. In sharp contrast, halide SSEs, particularly Zr-based halides such as LZCO, are markedly sensitive to organic solvents, and a systematic assessment of solvent-halide compatibility remains lacking [25]. This paucity of systematic studies hampers processability and constrains interfacial design in halide-based composite cathodes. Accordingly, establishing solvent-compatibility criteria and identifying halide-tolerant organic solvents are essential to advancing halide SSBs.

In this study, we propose an innovative interfacial strategy that employs functional organic molecules as cathode electrolyte interphase (CEI)-forming additives and systematically assess their chemical compatibility with LZCO. On the basis of failure-mechanism screening, we identify perfluoropolyether (PFE), a highly fluorinated liquid, as a uniquely stable CEI-forming additive for halide SSEs. Owing to its low volatility, high wettability, and intrinsic nonflammability, PFE is readily incorporated into composite cathodes via dry-electrode processing without compromising the inherent safety of SSBs. During cycling, PFE reacts with deintercalated Li^+ to form an organic-inorganic hybrid cathode electrolyte interphase (CEI) composed of fluoropolyether species and LiF. Benefiting from its high Li^+ conductivity and conformal coverage, the PFE-derived CEI converts localized point contacts into CEI-mediated areal contacts at the LZCO-$LiNi_{0.82}Co_{0.14}Mn_{0.04}O_2$ (Ni82) interphase, thereby improving interfacial Li^+ transport and reducing the fraction of previously electrochemically inactive Ni82. The chemically robust CEI concurrently suppresses parasitic reactions, including SSEs oxidation, O_2 evolution, rock-salt phase reconstruction, and Li/Ni mixing. Consequently, PFE-containing composite cathodes deliver high specific capacity, excellent rate capability, and durable cycling stability. Moreover, pouch-cell validation underscores the practical feasibility of PFE for commercially relevant SSBs applications.

2 | Results and Discussion

2.1 | Capability of the PFE Additive in Halide-Based Composite Cathodes

In view of the scarcity of prior studies on CEI-forming additives for halide-based composite cathodes, this work establishes design criteria for such additives, informed by the intrinsic properties of halide SSEs and the requirements for electrode fabrication: (i) chemical compatibility with halide SSEs; (ii) uniform dispersion within composite cathodes; (iii) ability to form a robust, stable CEI; and (iv) preservation of the inherent safety of composite cathodes. In conventional LIBs, widely used salt-type CEI-forming additives (e.g., lithium difluorophosphate ($LiPF_2O_2$), lithium difluoro(oxalato)borate (LiDFOB)) [26, 27] are readily soluble in liquid electrolytes with aprotic solvents but exhibit poor solubility in low-polarity solvents (e.g., toluene, xylene) that are typically used in slurry-based (wet-electrode) processing of composite cathodes [28–30]. When added directly as solid particulates to composite cathodes, these additives form rigid, nonconformal contact with cathode surfaces, hindering the realization of their interfacial functionality. By contrast, liquid CEI-forming additives can be uniformly delivered via dry-electrode processing and can readily wet cathode surfaces. Accordingly, representative liquid CEI-forming additives were selected in this work, and their chemical compatibility with the LZCO was systematically investigated.

As shown in Figures S1–S6, immersion of LZCO in commonly used CEI-forming additives, including fluoroethylene carbonate (FEC) [31], triallyl phosphate (TAP) [32], tris(trimethylsilyl) phosphate (TMSP) [33], tris(trimethylsilyl) phosphite (TMSPi) [34], trimethyl borate (TMB) [35], and ethylene sulfite (ES) [36], leads to structural degradation and a marked decrease in its ionic conductivity. This degradation arises from nucleophilic attack by Lewis-basic oxygen (O) atoms in these additives at the strongly Lewis-acidic zirconium (Zr) centers in LZCO [3, 25]. By contrast, LZCO immersed in 2,2,2-trifluoroethyl 1,1,2,2-tetrafluoroethyl ether (TTE) or 1,1,2,2-tetrafluoroethyl-2,2,3,3-tetrafluoropropylether (HFE) retains its crystallinity and high ionic conductivity (Figures S7 and S8) [37, 38]. This chemical stability is attributed to the strong electron-withdrawing effect of fluorinated substituents in TTE and HFE, which lowers the nucleophilicity of the O atoms and thereby suppresses the Lewis acid-base reactions with LZCO [39]. Nevertheless, these fluorinated small-molecule solvents are highly volatile [40], making it difficult to precisely control additive loading and ensure uniform distribution within composite cathodes during dry-electrode processing.

Employing liquid PFE offers an effective strategy to mitigate the volatility of low-molecular-weight fluorinated ethers (Figure 1a). Like TTE and HFE, PFE contains abundant C—F bonds, which can promote the formation of an F-rich CEI, thereby making PFE a promising CEI-forming additive [41, 42]. Furthermore,

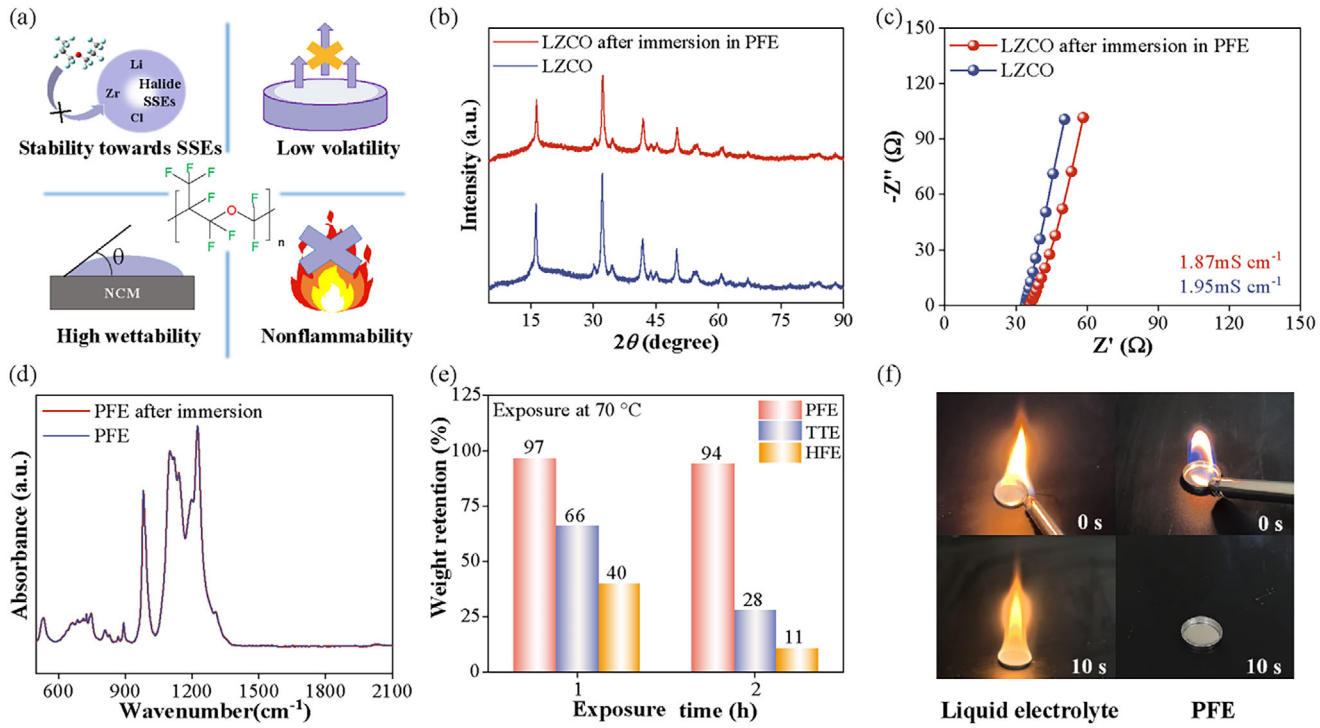

FIGURE 1 | (a) schematic of the molecular structure and physicochemical properties of PFE; (b) XRD patterns of LZCO before and after immersion in PFE; (c) EIS spectra and corresponding ionic conductivities of LZCO before and after immersion in PFE; (d) FTIR spectra of pristine PFE and PFE after immersion; (e) weight retention of PFE, TTE, and HFE after 1 and 2 h of uncovered exposure at 70°C; (f) ignition tests comparing a liquid electrolyte (12 wt.% $LiPF_6$ + 25 wt.% ethylene carbonate + 63 wt.% diethyl carbonate) with PFE.

X-ray diffraction (XRD) patterns and electrochemical impedance spectroscopy (EIS) spectra of LZCO before and after immersion in PFE reveal no detectable structural change and only a slight decrease in ionic conductivity of LZCO (Figure 1b,c). Moreover, the Fourier transform infrared (FTIR) spectra of PFE after immersion and pristine PFE are essentially identical, indicating preservation of its molecular structure (Figure 1d).

The volatility of PFE was further evaluated at a representative roll-pressing temperature (70°C) commonly used during dry-electrode processing and was benchmarked against those of TTE and HFE [43, 44]. As shown in Figure 1e, approximately 94 wt.% of PFE remained after 2 h of uncovered exposure at 70°C, in stark contrast to TTE (28 wt.%) and HFE (11 wt.%), thereby confirming the substantially lower volatility of PFE. Moreover, despite its high molecular weight, PFE still exhibits lower surface tension (1.24 mN m^{-1}) and a lower contact angle (6.24°) than those of a representative electrolyte for conventional LIBs (1.38 mN m^{-1}, 8.92°; Table S1), thereby promoting excellent wettability and enabling uniform dispersion within composite cathodes during dry-electrode processing. Additionally, owing to its extensive fluorination, PFE is intrinsically nonflammable (Figure 1f), helping to preserve the inherent safety of SSBs when used as an additive. Taken together, PFE's chemical stability toward halide SSEs, low volatility, excellent wettability, and intrinsic nonflammability highlight its potential as a CEI-forming additive for halide-based composite cathodes.

2.2 | Enhancing the Electrochemical Performance of Composite Cathodes with PFE

Herein, Ni82 was employed as the cathode active material. Composite cathodes were prepared by uniformly mixing Ni82, LZCO, PFE, and vapor-grown carbon fibers (VGCF) by grinding, followed by pellet pressing. Half-cells were assembled with a Li-In alloy as both the counter and reference electrodes to evaluate the electrochemical performance of the composite cathodes (Figure S9). Hereafter, the composite cathode without PFE is denoted NCM, and that containing 5 wt.% PFE is denoted NCM@PFE. During the initial charge–discharge cycle at 0.1C (1C = 200 mA g^{-1}), NCM@PFE delivered a specific capacity of 206 mAh g^{-1} (based on the mass of Ni82), exceeding that of NCM (186 mAh g^{-1}) under identical conditions (Figure 2a). Even at an ultra-low rate of 0.02C, the specific capacity of NCM@PFE (210 mAh g^{-1}) remained markedly higher than that of NCM (193 mAh g^{-1}), suggesting that incorporating PFE reduces the electrochemically inactive fraction of Ni82 [45]. In addition to its higher capacity, NCM@PFE exhibited enhanced rate capability relative to NCM. At 0.2C, 0.5C, and 1C, the capacity retentions of NCM@PFE were 98%, 88%, and 76%, respectively, exceeding those of NCM at the corresponding rates (Figure 2b; Figure S10).

Besides, NCM@PFE exhibited improved cycling stability, retaining 83% of its initial capacity after 1 500 cycles at 0.5C, significantly higher than NCM (36%). The capacity fade during cycling can be attributed to two primary factors: (i) the progressive accumulation of electrochemically inactive Ni82, arising from

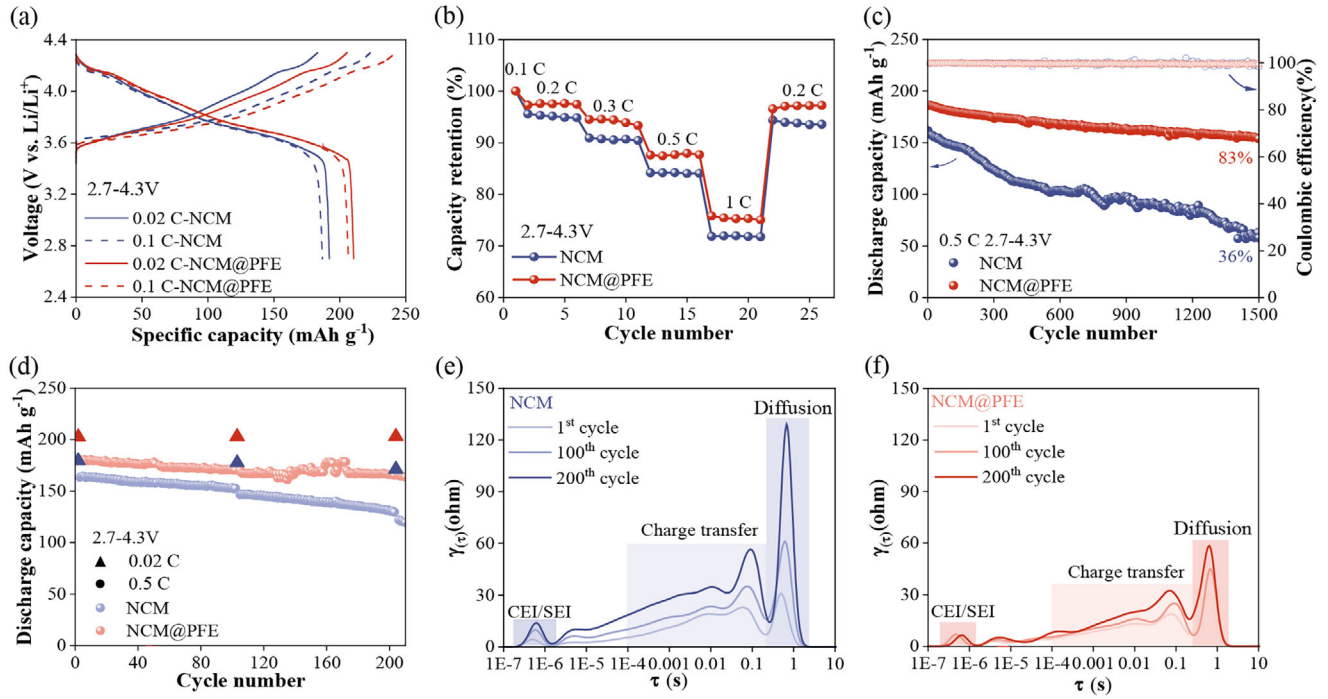

FIGURE 2 | (a) charge–discharge curves of NCM and NCM@PFE at 0.1C and 0.02C; (b) rate performance of NCM and NCM@PFE; (c) cycling stability of NCM and NCM@PFE at 0.5C; (d) discharge capacities versus cycle number, assessed by a single 0.02C diagnostic cycle after every 100 cycles at 0.5C; (e,f) DRT spectra obtained from EIS for (e) NCM and (f) NCM@PFE at selected cycle counts.

mechanical loss of contact at the Ni82-LZCO interface and from structural distortions of Ni82; (ii) increased charge–discharge polarization, which hinders part of the active Ni82 from participating in redox reactions under identical C-rates and cutoff voltages [46]. To decouple the relative contributions of inactive Ni82 accumulation and polarization growth to capacity fade during cycling, diagnostic charge–discharge tests at 0.02C were performed after selected cycle counts [47]. As shown in Figure 2d and Figure S11, after 100 and 200 cycles at 0.5C, the capacity retention of NCM decreased to 93.4% and 79.3%, respectively. When subsequently measured at 0.02C to minimize the effect of polarization on the capacity, the corresponding capacities recovered to 99.0% and 95.4% of the initial 0.02C capacity, respectively. In contrast, after 200 cycles, NCM@PFE retained 91.9% at 0.5C, while its capacity at 0.02C recovered to 100%, indicating negligible accumulation of electrochemically inactive Ni82. These results indicate that polarization growth dominates capacity fade at 0.5C and that PFE mitigates both polarization growth and the accumulation of electrochemically inactive Ni82 during cycling.

Furthermore, EIS (Figure S12), together with the corresponding distribution of relaxation times (DRT) analysis (Figure 2e,f), were employed to elucidate the impedance evolution in the composite cathodes during cycling. On the basis of the distinct relaxation times (τ) of individual electrochemical processes, three characteristic regions were unambiguously resolved in the DRT spectra from NCM and NCM@PFE, corresponding to the interfacial resistance ($R_{CEI/SEI}$), charge-transfer resistance (R_{ct}), and diffusion resistance (R_D), with R_{ct} and R_D providing the dominant contributions [48, 49]. Notably, at the first cycle, NCM@PFE exhibited lower R_{ct} and R_D than NCM, consistent with its enhanced rate capability. Furthermore, after 100 and 200 cycles, the increases in R_{ct} and R_D for NCM@PFE were substantially suppressed compared with NCM, indicating that the incorporation of PFE effectively limits impedance growth and the corresponding charge–discharge polarization during cycling.

Under a more practical constant current (CC)-constant voltage (CV) charging mode (CC to 4.3 V at 0.5C, followed by CV at 4.3 V until the current decreased to 0.02C), NCM@PFE delivered a substantially higher capacity retention of 82% after 500 cycles, compared with only 40% for NCM under the same conditions (Figure S13). Notably, during cycling, the contribution of the CV step to the total charge gradually increased for both NCM and NCM@PFE, consistent with impedance growth. However, after 500 cycles, the CV contribution for NCM@PFE (42%) remained substantially lower than that of NCM (69%), further supporting the conclusion that the incorporation of PFE effectively suppresses impedance growth during cycling. Additionally, composite cathodes containing 2.5, 7.5, and 10 wt.% PFE also exhibited improvements in specific capacity and cycling stability, with 5 wt.% PFE delivering the optimal electrochemical performance among the compositions tested (Figure S14). Overall, the incorporation of PFE into composite cathodes not only reduces impedance and the fraction of electrochemically inactive Ni82 but also suppresses their subsequent growth during cycling. Consequently, NCM@PFE exhibits higher specific capacity, superior rate capability, and markedly enhanced cycling stability compared with NCM.

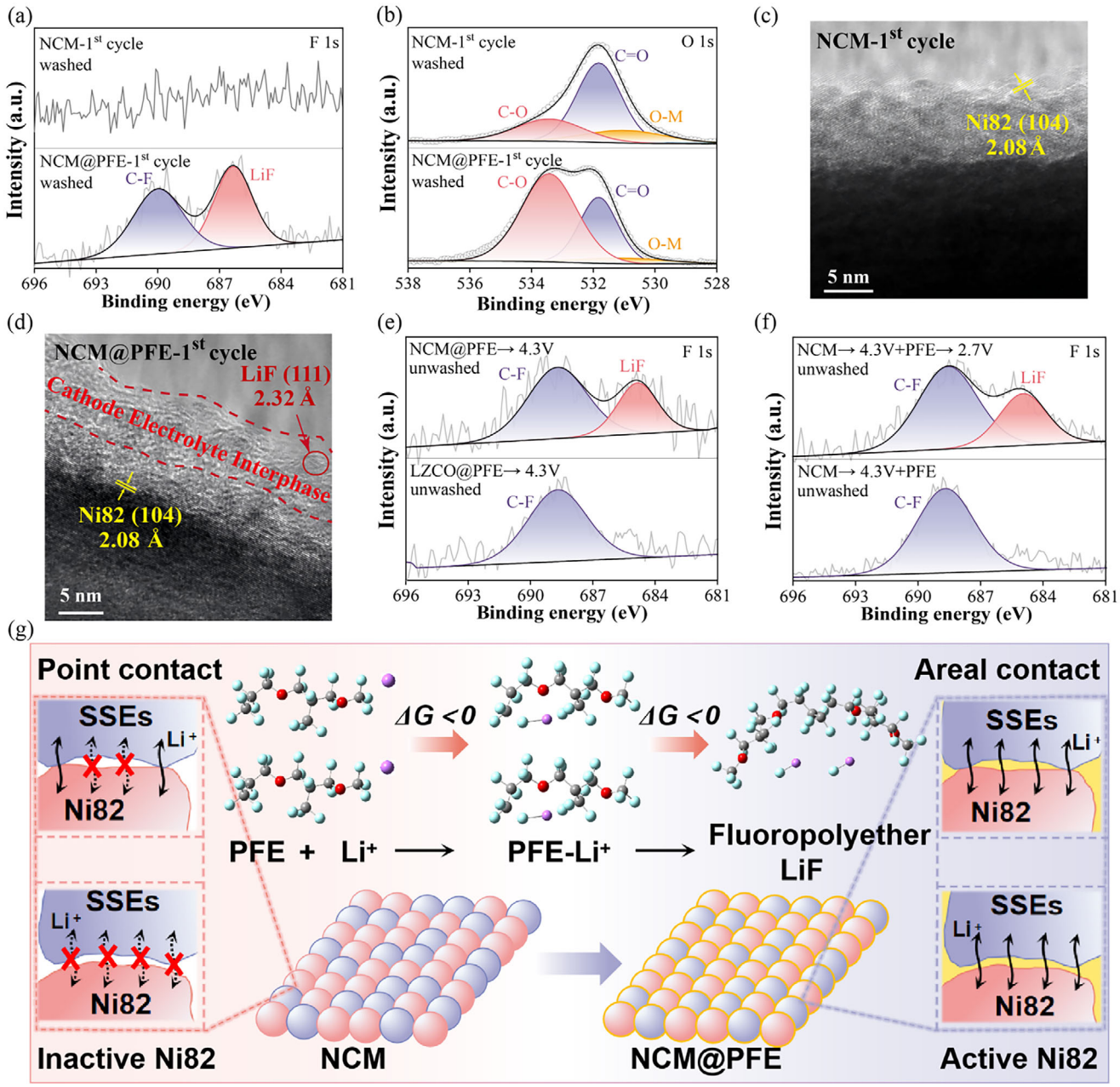

FIGURE 3 | (a) F 1s and (b) O 1s XPS spectra of washed NCM and NCM@PFE electrodes after one charge–discharge cycle; (c) HRTEM images of Ni82 particles in washed (c) NCM and (d) NCM@PFE after one charge–discharge cycle; (e) F 1s XPS spectra of NCM@PFE and LZCO@PFE after LSV to 4.3 V; (f) F 1s XPS spectra of fully charged NCM composite cathodes: (i) immersed in PFE and subsequently discharged to 2.7 V via LSV, (ii) immersed in PFE only; (g) schematic of PFE-derived CEI formation and interfacial contact evolution in composited cathodes.

2.3 | Mechanisms for Enhanced Performance of NCM@PFE

By analogy with the CEI-forming additives TTE and HFE, PFE is hypothesized to improve the electrochemical performance of composite cathodes via a similar CEI-forming mechanism. To evaluate this hypothesis, X-ray photoelectron spectroscopy (XPS) was performed on composite cathodes at selected charge–discharge states after sequential washing in dimethyl carbonate (DMC) followed by pivalonitrile. Because DMC both decomposes and dissolves a substantial fraction of LZCO (Figure S15), while pivalonitrile dissolves PFE, this cleaning protocol affords more complete exposure of the Ni82 surface. As shown in Figure 3a and Figure S16, no F 1s signal was detected in the spectra of either once-cycled NCM or uncycled NCM@PFE. By contrast, once-cycled NCM@PFE exhibited distinct C-F and LiF peaks in the F 1s region [50], consistent with the formation of a CEI comprising fluorinated organic species and LiF. Moreover, compared with NCM, the O 1s spectrum of NCM@PFE exhibited a pronounced increase in the C-O contribution, accompanied by marked decreases in the C═O and O─M (M = metal) peaks (Figure 3b) [51], consistent with an organic CEI enriched in

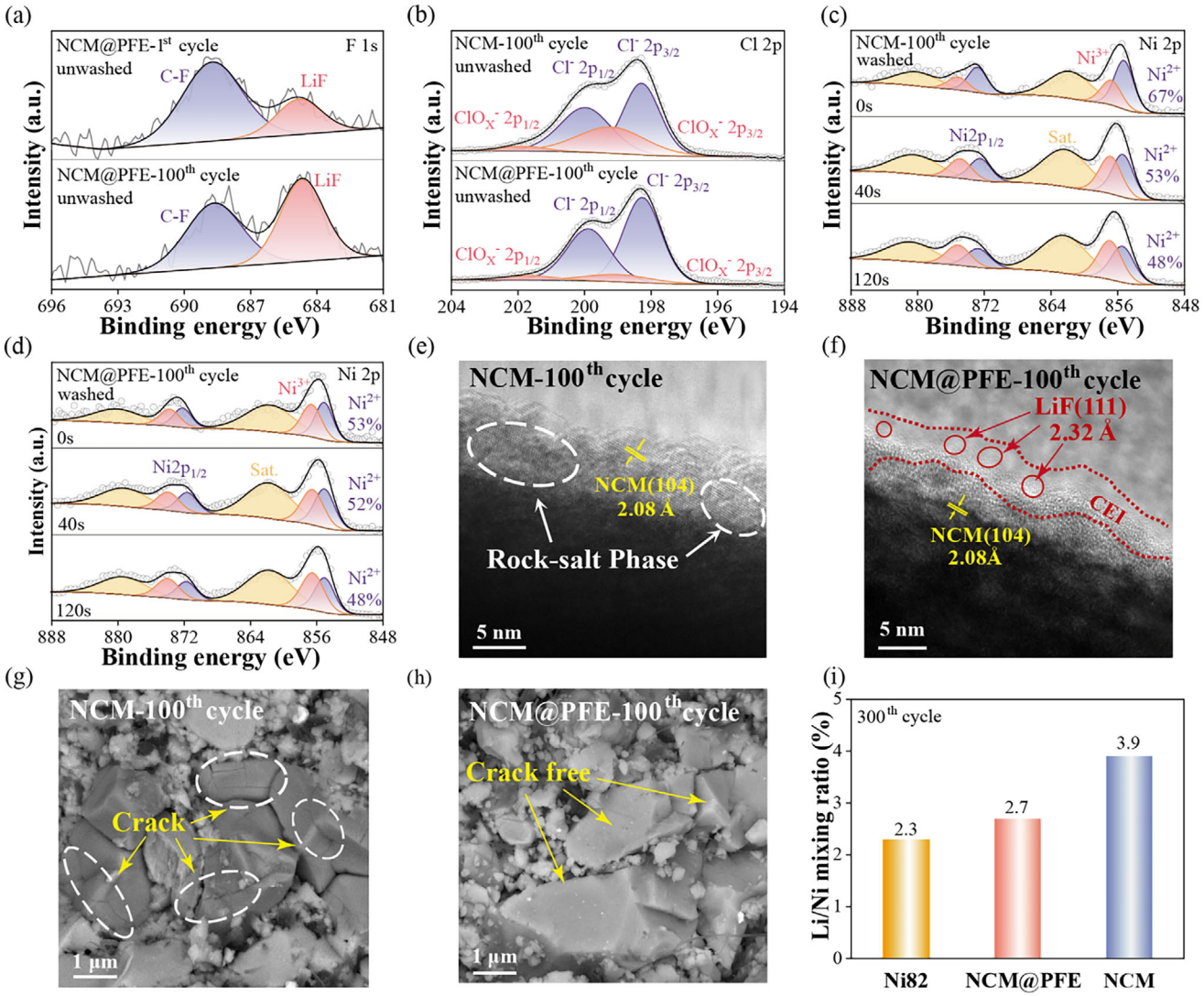

FIGURE 4 | (a) F 1s XPS spectra of NCM@PFE after 1 and 100 cycles; (b) Cl 2p XPS spectra of NCM and NCM@PFE after 100 cycles; (c,d) Ni 2p XPS spectra of (c) NCM and (d) NCM@PFE after 100 cycles with Ar^+ sputter depth profiling; (e,f) HRTEM images of Ni82 particles in (e) NCM and (f) NCM@PFE after 100 cycles; (g,h) SEM images of (g) NCM and (h) NCM@PFE after 100 cycles; (i) Li/Ni mixing ratios for pristine Ni82 powder and for Ni82 in NCM and NCM@PFE after 300 cycles.

high-molecular-weight, insoluble fluoropolyether species formed during cycling.

High-resolution transmission electron microscopy (HRTEM) of the washed Ni82 particles revealed the formation of a PFE-derived CEI (Figure 3c,d). After the first charge–discharge cycle, Ni82 particles in NCM@PFE are uniformly coated with a ≈6-nm-thick CEI, whereas no comparable coating was observed on Ni82 particles in NCM. HRTEM further shows that the CEI is composed primarily of amorphous fluoropolyether species, within which LiF nanocrystals are randomly dispersed. Taken together, these observations indicate that PFE promotes the formation of a fluoropolyether-LiF hybrid CEI layer on Ni82 surfaces.

To further elucidate the formation mechanism of the PFE-derived CEI, we performed XPS on the electrode surfaces subjected to various electrochemical or chemical treatments. Because the positions of the C-F and other characteristic peaks of the fluoropolyether species in the CEI overlap with those of PFE in the XPS spectra (Figure S17), CEI formation is assessed by the presence or absence of the LiF peak. Following linear sweep voltammetry (LSV, Figure S18a) to 4.3 V, a distinct LiF component was detected in the F 1s spectrum of NCM@PFE, confirming CEI formation (Figure 3e). By contrast, for the Ni82-free LZCO@PFE electrode (LZCO:VGCF:PFE = 70:30:5), LSV to 4.3 V yielded no detectable LiF component in the F 1s spectrum (Figure 3e). Consistent with the XPS results, the LSV curve of the LZCO@PFE electrode showed no additional anodic peak compared with the LZCO electrode (LZCO:VGCF = 70:30) (Figure S18b). Moreover, after a fully charged NCM composite cathode was immersed in PFE and subsequently discharged to 2.7 V via LSV, a LiF peak was also detected in the F 1s spectrum (Figure 3f). By contrast, simply mixing a fully charged NCM cathode with PFE yielded no detectable LiF peak in the F 1s spectrum (Figure 3f). Additionally, when Ni82 in the composite cathode was replaced with $LiFePO_4$

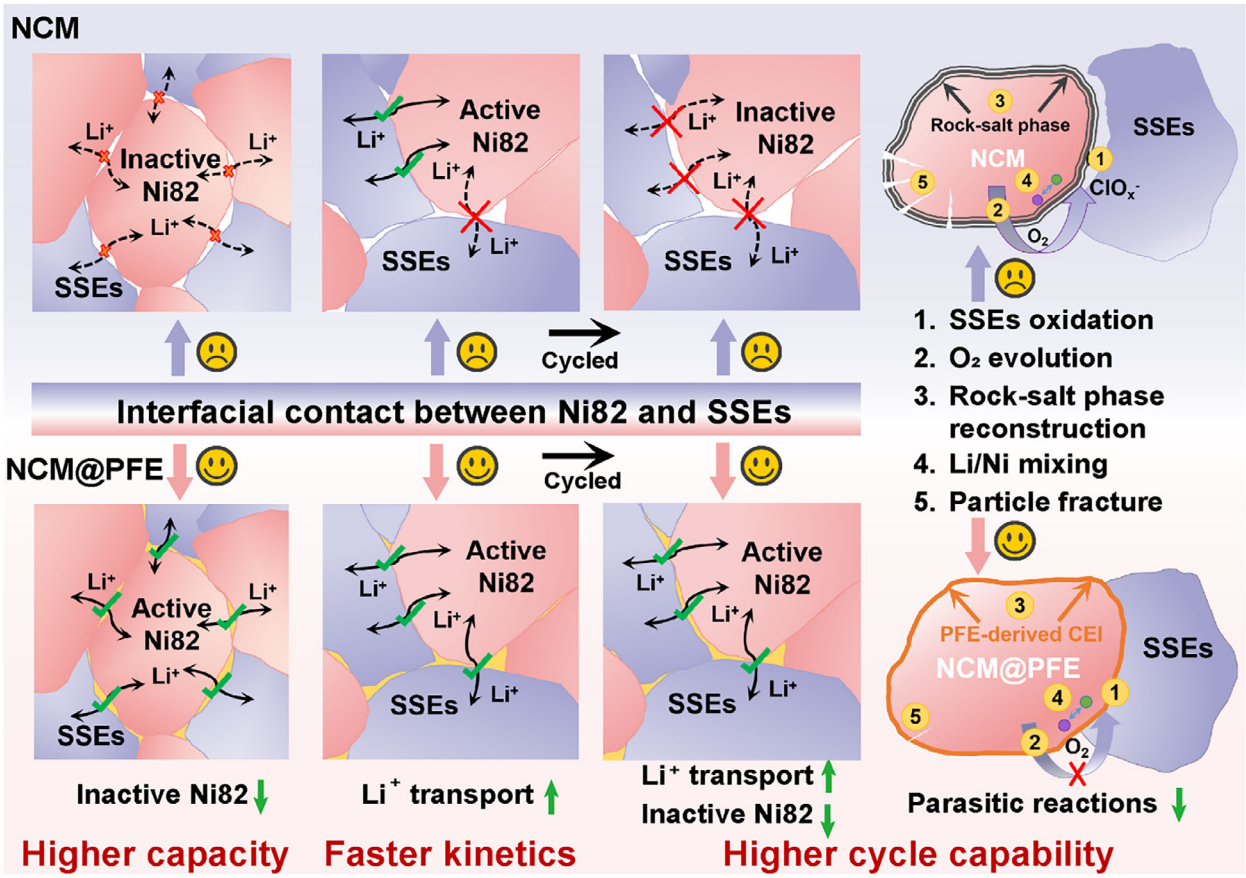

FIGURE 5 | Schematic of the performance enhancement mechanism of NCM@PFE.

and $LiNi_{0.5}Mn_{1.5}O_4$, PFE-derived CEI formation was observed in all cases following LSV to the fully charged state (Figures S19 and S20).

Taken together, these results indicate that neither chemical oxidation by fully charged Ni82 nor electrochemical oxidation alone is sufficient to initiate CEI formation. CEI formation occurs only when both charging and discharging are carried out in composite cathodes, regardless of the cathode active material. Given the abundant interfacial Li^+ flux during both oxidation and reduction, we propose that the PFE-derived CEI is initiated by an interfacial reaction between deintercalated Li^+ and PFE. By contrast, the negligible current observed during LSV of the LZCO@PFE electrode (Figure S18) indicates that the interfacial Li^+ flux available for reaction with PFE is negligible, thereby precluding interfacial LiF formation.

Density functional theory (DFT) calculations corroborate the formation mechanism of the PFE-derived CEI. As shown in Figure 3g and Figure S21, Li^+ coordination at all F sites on model PFE fragments was systematically sampled, and the Gibbs free energies (ΔG) of the resulting structures were computed for thermodynamic analysis. The results show that coordination of Li^+ to F atoms in PFE facilitates the minimization of system energy, indicating that Li^+ tends to bind to F atoms in PFE. Furthermore, LiF elimination from these Li^+-coordinated PFE fragments, followed by coupling of two defluorinated PFE fragments, proceeds with an overall negative ΔG, demonstrating an energetically favorable pathway to form LiF and fluoropolyether.

To further validate this conclusion, we introduced 5 wt.% PFE into the LZCO halide electrolyte layer of an NCM based SSBs, denoted as LZCO+PFE. After one charge and discharge cycle, the cycled electrolyte interlayer was examined by XPS. As shown in Figure S22, a clear LiF component emerges in the F 1s spectrum of the electrolyte layer. This observation indicates that LiF rich interphase formation does not require an electrochemical redox process, but can be triggered when deintercalated Li^+ come into contact with PFE.

In PFE-derived CEI, the organic fluoropolyether component affords high chemical stability, rapid Li^+ transport, and mechanical compliance [52, 53], thereby accommodating volume changes of the Ni82 cathode during cycling and mitigating CEI fracture. Concurrently, the inorganic LiF domains confer mechanical reinforcement, high oxidative stability, and electronic insulation [54, 55]. Importantly, when the inorganic LiF and organic components coexist in an intimate hybrid architecture, Li^+ migration can proceed with a reduced energy barrier, suggesting that organic–inorganic interfacial regions facilitate accelerated Li^+ transport [56, 57]. Consequently, the PFE-derived CEI synergistically integrates high oxidative stability, rapid Li^+ conduction, mechanical robustness, and elasticity.

It is widely recognized that in composite cathodes, the contact between active material particles and SEEs is predominantly point-like (Figure 3g) [44, 58]. Therefore, NCM is limited by sluggish Li^+ transport at the Ni82-LZCO interface. Additionally, insufficient Ni82-LZCO interfacial contact leaves a substantial

fraction of particles electrochemically inactive. In contrast, in NCM@PFE, an in situ CEI forming on the surface of Ni82 particles fills interfacial voids at the Ni82-LZCO interfaces, thereby converting point contacts into CEI-mediated areal contacts. Consequently, in NCM@PFE, Li^+ transfers efficiently across the Ni82-LZCO interface via Li^+-conductive CEI, thereby markedly enhancing interfacial ion-transport kinetics.

To further corroborate the PFE enabled kinetic enhancement, Galvanostatic Intermittent Titration Technique(GITT) and variable scan rate Cyclic Voltammetry (CV) measurements were performed on the composite cathodes. The diffusion coefficient derived from GITT reflects the electrochemical dynamics and polarization behavior of the composite electrode and thus the effective Li^+ transport within the composite cathode. As shown in Figure S23, NCM@PFE displays reduced polarization and markedly higher Li^+ diffusivity than the NCM cathode. Consistently, the variable scan rate CV results in Figure S24 show a substantially smaller peak potential shift for NCM@PFE with increasing scan rate, indicative of improved reaction kinetics and mitigated polarization. Collectively, these GITT and CV results, together with the EIS data, demonstrate that introducing PFE enhances interfacial Li^+ transport and reduces polarization in the composite cathode.

Additionally, the CEI creates continuous ion-conducting pathways that reconnect previously inactive Ni82 particles to the percolation network, effectively reactivating them for electrochemical cycling. Collectively, the PFE-derived CEI improves Ni82 utilization and increases specific capacity, while markedly enhancing the electrochemical kinetics in composite cathodes. To further elucidate the mechanism by which the PFE-derived CEI enhances cycling stability, XPS was performed on NCM@PFE electrodes before and after cycling. After 100 cycles, the LiF component in the F 1s spectrum (Figure 4a) increased substantially, indicating ongoing CEI growth accompanied by progressive LiF accumulation. Thermogravimetric analysis (Figure S25) further revealed that the mass loss of NCM@PFE at 250°C decreased from 4.6% (before cycling) to 3.5% (after the first cycle) and then to 2.2% (after 100 cycles), consistent with progressive conversion of PFE into nonvolatile fluoropolyether species and LiF during CEI formation. These observations collectively indicate that PFE is not depleted during the initial cycle. The residual PFE serves as a self-healing reservoir, continuously repairing freshly exposed Ni82 surfaces arising from CEI cracking or particle fracture, thereby preserving interphase integrity. This dynamic CEI-forming process maintains CEI-mediated areal contact between Ni82 and LZCO particles, sustains continuous Li^+ transport pathways, and suppresses interfacial impedance growth as well as the accumulation of inactive Ni82 during cycling.

Further analysis revealed that in the XPS spectra of NCM and NCM@PFE after 100 cycles (Figure 4b), oxidized chlorine species $ClOx^-$ appeared [59], indicating that LZCO undergoes oxidative side reactions during cycling. To pinpoint the oxygen source in $ClOx^-$, oxygen-free Li_2ZrCl_6 (LZC) was employed to prepare composite cathodes in lieu of LZCO. Under identical testing conditions, the Cl 2p spectrum of the LZC-based composite cathode likewise revealed $ClOx^-$ (Figure S26), indicating that the oxygen incorporated into $ClOx^-$ originated not from LZCO but from highly reactive oxygen (O_2) evolved from the Ni82 cathode during cycling [60, 61]. In conventional LIBs with liquid electrolyte, O_2 oxidizes the electrolyte, causing solvent decomposition and compromising cycling stability [62]. In composite cathodes with halide SSEs, O_2 likewise oxidizes LZCO or LZC, thereby damaging the structure of the halide SSEs, reducing their ionic conductivity, and ultimately degrading overall cell-level cycling performance [24, 63]. Moreover, relative to NCM, the $ClOx^-$ peak intensity after cycling was markedly reduced in NCM@PFE, suggesting that the CEI on Ni82 suppressed O_2 evolution and mitigates oxidative degradation of the halide SSEs. Additionally, after 100 cycles, the NCM and NCM@PFE composite cathodes were washed to remove LZCO and residual PFE, and the recovered Ni82 particles were then analyzed by XPS using Ar^+ sputter depth profiling. As shown in Figure 4c, Ni82 in cycled NCM exhibits a surface Ni^{2+} fraction of 67% in the Ni 2p spectrum, substantially higher than the 48% measured in the bulk-like region. This marked surface-bulk disparity indicates extensive rock-salt phase transformation at the Ni82 particle surface [64]. In contrast, in Ni82 protected by the CEI (Figure 4d), the surface Ni^{2+} fraction is 53%, comparable to the bulk value (48%), suggesting effective suppression of the rock-salt phase transformation. This conclusion is further corroborated by HRTEM images (Figure 4e,f), in which cycled NCM exhibits pronounced rock-salt domains on Ni82 surfaces, whereas CEI-protected Ni82 exhibits no discernible rock-salt phase [65]. This surface reconstruction not only consumes active material and impedes Li^+ transport but also induces internal stress accumulation during cycling due to the volumetric mismatch between the rock-salt and layered phases, ultimately leading to particle fracture [66]. This degradation pathway is further corroborated by SEM images (Figure 4g,h). After 100 cycles, Ni82 particles in the NCM exhibit extensive surface cracking, while those in NCM@PFE largely maintain their structural integrity.

Additionally, XRD measurements were conducted on uncycled NCM and on cycled and washed NCM/NCM@PFE, Additionally, XRD was performed on pristine NCM, as well as on cycled NCM and NCM@PFE after DMC washing, and subsequent Rietveld refinement was used to quantify the extent of Li/Ni mixing [67]. As shown in Figure 4i and Figure S27, the Li/Ni mixing ratio of unprotected Ni82 increased from 2.3% to 3.9% after 300 cycles, whereas CEI-protected Ni82 under identical conditions showed a Li/Ni mixing ratio of only 2.7%. Suppressing Li/Ni mixing curtails active material loss and preserves Li^+ diffusion coefficients, thereby enhancing cycling stability of Ni82 [68, 69].

The mechanisms through which the CEI enhances the electrochemical performance of the composite cathode are schematically illustrated in Figure 5. The in situ-formed CEI converts the Ni82-LZCO contact from point contacts to CEI-mediated areal contacts. The Li^+-conductive CEI extends ion-transport pathways, thereby enhancing interfacial ion-transport kinetics and reducing the fraction of electrochemically inactive Ni82. Consequently, the composite cathode exhibits higher specific capacity and faster reaction kinetics. During cycling, the high elasticity of the PFE-derived CEI, together with the dynamic film-forming behavior of PFE, maintains CEI-mediated areal contacts, thereby ensuring steady interfacial Li^+ transport and suppressing the accumulation of electrochemically inactive Ni82. Concurrently, the PFE-derived CEI suppresses interfacial side reactions at the Ni82-LZCO interface, thereby limiting O_2-induced LZCO

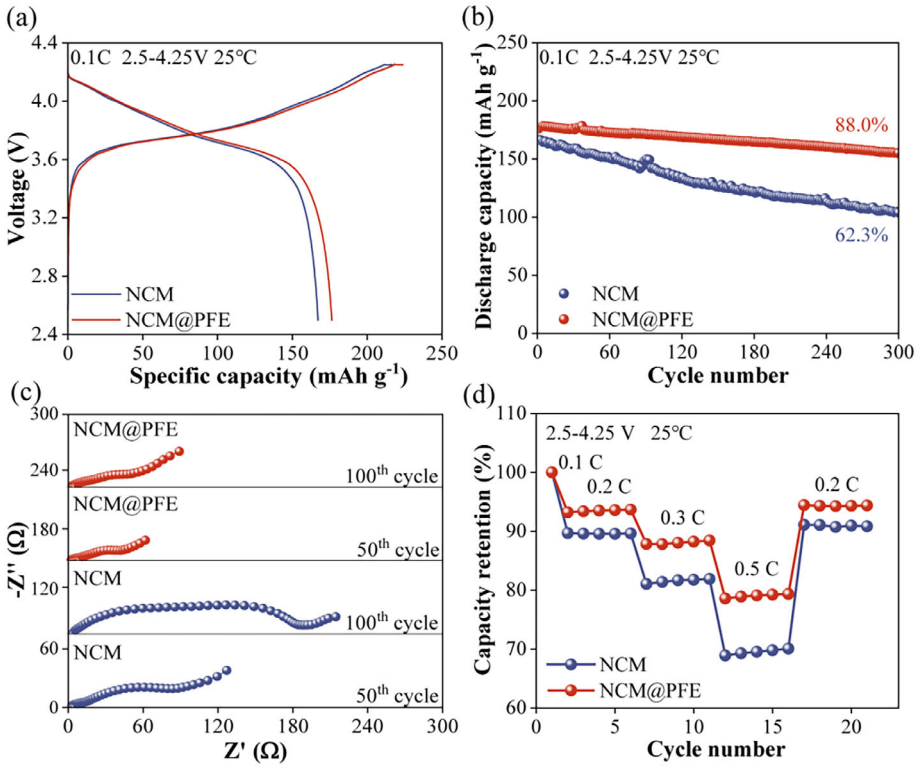

FIGURE 6 | (a) charge–discharge curves of pouch cells at 0.1C; (b) cycling performance of pouch cells at 0.1C; (c) EIS of pouch cells at selected cycle counts; (d) pouch cells rate performance of NCM and NCM@PFE.

oxidation as well as rock-salt phase transformation, Li/Ni mixing, and particle fracture of Ni82. Consequently, the PFE-derived CEI maintains the Li^+-transport network within the composite cathode and mitigates side reactions at both the LZCO and Ni82 interfaces, thereby improving cycling stability.

2.4 | Application in Solid-State Pouch Cells

To further assess the practical feasibility of PFE, solid-state pouch cells were assembled with Ag-C anodes and either NCM or NCM@PFE composite cathodes (Figure S28). As shown in Figure 6a,b, incorporating PFE raises the specific capacity at 0.1C from 167 to 176 mAh g^{-1} (based on the mass of Ni82), and improves capacity retention after 300 cycles increases from 62.3% to 88.0%. Moreover, PFE-containing pouch cells consistently exhibit lower impedance throughout cycling (Figure 6c). In addition, NCM@PFE delivers improved rate capability relative to NCM. At 0.2C, 0.3C, and 0.5C, NCM@PFE retains 93%, 88%, and 79% of its capacity, respectively, which is consistently higher than NCM at the same rates (Figure 6d and Figure S29). Notably, even at the higher rate of 0.3C, the incorporation of PFE still enhances cycling stability (Figure S30). These results underscore the practical potential of PFE for practical solid-state pouch cells.

3 | Conclusion

In this work, we introduce PFE as a CEI-forming additive for halide-based composite cathodes. PFE exhibits excellent chemical stability toward halide SSEs and intrinsic nonflammability. Given its high boiling point and excellent wettability, PFE can be homogeneously incorporated into composite cathodes through dry-electrode processing. During cycling, PFE forms a fluoropolyether-LiF hybrid CEI by reacting with deintercalacted Li^+. This Li^+-conductive, conformal CEI transforms localized point contacts at the Ni82-LZCO interface into CEI-mediated areal contacts, thereby enhancing the Li^+-transport network and reactivating previously electrochemically inactive Ni82 particles. The robust CEI also suppresses parasitic reactions, including LZCO oxidation, as well as O_2 evolution, rock-salt reconstruction, Li/Ni mixing, and particle fracture of Ni82 particles. Composite cathodes containing PFE deliver exceptional performance, achieving 206 mAh g^{-1} at 0.1C, retaining 76% at 1C and 83% after 1500 cycles at 0.5C. Pouch-cell validation further highlighting the potential of PFE for practical SSBs applications.

Acknowledgements

This work was supported by the National Natural Science Foundation of China (nos. 52162028 and 52371214), the Natural Science Foundation of Jiangxi Province (nos. 20232ACB204011 and 20224BAB204001), the Major Research Program of Jingdezhen Ceramic Industry (no. 2023ZDGG001), the State Key Laboratory of New Ceramic Materials Tsinghua University (nos. KF202309 and KF202414), the Jiangsu Province Frontier Technology Research and Development Project (no. BF2024033), the Suzhou Science and Technology Program Project (no. ZXL2023236) and the Jiangsu Provincial Basic Research Program (BK20250539).

Conflicts of Interest

The authors declare no conflicts of interest.

Data Availability Statement

The data that support the findings of this study are available from the corresponding author upon reasonable request.

References

1. J. Janek and W. G. Zeier, "A Solid Future for Battery Development," *Nature Energy* 1 (2016): 16141, https://doi.org/10.1038/nenergy.2016.141.

2. X. Ji, Y. Zhang, M. Cao, et al., "Advanced Inorganic/Polymer Hybrid Electrolytes for all-Solid-State Lithium Batteries," *Journal of Advanced Ceramics* 11 (2022): 835–861, https://doi.org/10.1007/s40145-022-0580-8.

3. K. Tuo, C. Sun, and S. Liu, "Recent Progress in and Perspectives on Emerging Halide Superionic Conductors for all-Solid-State Batteries," *Electrochemical Energy Reviews* 6 (2023): 17, https://doi.org/10.1007/s41918-023-00179-5.

4. X. Zhang, H. Yi, Y. Shi, et al., "Low-Cost High-Air-Stability Argyrodite Electrolyte Delivering Excellent Interface Compatibility in all-Solid-State Lithium Metal Batteries," *Energy Storage Materials* 83 (2025): 104689, https://doi.org/10.1016/j.ensm.2025.104689.

5. X. Nie, J. Hu, and C. Li, "Halide-Based Solid Electrolytes: the History, Progress, and Challenges," *Interdisciplinary Materials* 2 (2023): 365–389.

6. S. Yang, S. Y. Kim, and G. Chen, "Halide Superionic Conductors for all-Solid-State Batteries: Effects of Synthesis and Composition on Lithium-Ion Conductivity," *ACS Energy Letters* 9 (2024): 2212–2221, https://doi.org/10.1021/acsenergylett.4c00317.

7. Q. Wang, Y. Zhou, X. Wang, et al., "Designing Lithium Halide Solid Electrolytes," *Nature Communications* 15 (2024): 1050, https://doi.org/10.1038/s41467-024-45258-3.

8. S. Zhang, F. Zhao, L.-Y. Chang, et al., "Amorphous Oxyhalide Matters for Achieving Lithium Superionic Conduction," *Journal of the American Chemical Society* 146 (2024): 2977–2985, https://doi.org/10.1021/jacs.3c07343.

9. L. Hu, J. Wang, K. Wang, et al., "A Cost-Effective, Ionically Conductive and Compressible Oxychloride Solid-State Electrolyte for Stable All-Solid-State Lithium-based Batteries," *Nature Communications* 14 (2023): 3807, https://doi.org/10.1038/s41467-023-39522-1.

10. K. Wang, Q. Ren, Z. Gu, et al., "A Cost-Effective and Humidity-Tolerant Chloride Solid Electrolyte for Lithium Batteries," *Nature Communications* 12 (2021): 4410, https://doi.org/10.1038/s41467-021-24697-2.

11. Y. Tan, M. Beltran, J. Ke, et al., "Interfacial Challenges of Halide-Based all-Solid-State Batteries," *Advanced Energy Materials* 15 (2025): 2403986, https://doi.org/10.1002/aenm.202403986.

12. Y. Chen, J. Qian, K. Wang, L. Li, F. Wu, and R. Chen, "Cutting-Edge Developments at the Interface of Inorganic Solid-State Electrolytes," *Advanced Materials* 37 (2025): 2502653, https://doi.org/10.1002/adma.202502653.

13. L. Zhou, T.-T. Zuo, C. Y. Kwok, et al., "High Areal Capacity, Long Cycle Life 4 V Ceramic all-Solid-State Li-Ion Batteries Enabled by Chloride Solid Electrolytes," *Nature Energy* 7 (2022): 83–93, https://doi.org/10.1038/s41560-021-00952-0.

14. J. Yun, H. R. Shin, T. D. Hoang, et al., "Deciphering the Critical Degradation Factors of Solid Composite Electrodes with Halide Electrolytes: Interfacial Reaction versus Ionic Transport," *Energy Storage Materials* 59 (2023): 102787, https://doi.org/10.1016/j.ensm.2023.102787.

15. A. Zhang, J. Wang, R. Yu, et al., "Practical Application of Li-Rich Materials in Halide all-Solid-State Batteries and Interfacial Reactions between Cathodes and Electrolytes," *ACS Applied Materials & Interfaces* 15 (2023): 8190–8199, https://doi.org/10.1021/acsami.2c21569.

16. J. Wu, J. Li, and X. Yao, "Exploring the Potential of Halide Electrolytes for Next-Generation All-Solid-State Lithium Batteries," *Advanced Functional Materials* 35 (2025): 2416671, https://doi.org/10.1002/adfm.202416671.

17. L. Zhou, T. Zuo, C. Li, Q. Zhang, J. Janek, and L. F. Nazar, "Li_{3-x} Zr_X $(Ho/Lu)_{1-x}$ Cl_6 Solid Electrolytes Enable Ultrahigh-Loading Solid-State Batteries with a Prelithiated Si Anode," *ACS Energy Letters* 8 (2023): 3102–3111, https://doi.org/10.1021/acsenergylett.3c00763.

18. D. Lee, Z. Cui, J. B. Goodenough, and A. Manthiram, "Interphase Stabilization of $LiNi_{0.5}$ $Mn_{1.5}$ O_4 Cathode for 5 V-Class all-Solid-State Batteries," *Small* 20 (2024): 2306053, https://doi.org/10.1002/smll.202306053.

19. Y. Gao, S. Zhang, F. Zhao, et al., "Fluorinated Superionic Oxychloride Solid Electrolytes for High-Voltage All-Solid-State Lithium Batteries," *ACS Energy Letters* 9 (2024): 1735–1742, https://doi.org/10.1021/acsenergylett.3c02243.

20. Y. Ye, J. Geng, D. Zuo, et al., "High-Voltage Long-Cycling All-Solid-State Lithium Batteries with High-Valent-Element-Doped Halide Electrolytes," *ACS Nano* 18 (2024): 18368–18378, https://doi.org/10.1021/acsnano.4c02678.

21. Q. Shao, C. Yan, M. Gao, et al., "New Insights into the Effects of Zr Substitution and Carbon Additive on Li_{3-x} Er_{1-x} Zr_X Cl_6 Halide Solid Electrolytes," *ACS Applied Materials & Interfaces* 14 (2022): 8095–8105, https://doi.org/10.1021/acsami.1c25087.

22. J. Y. Kim, J. Park, M. J. Lee, et al., "Diffusion-Dependent Graphite Electrode for all-Solid-State Batteries with Extremely High Energy Density," *ACS Energy Letters* 5 (2020): 2995–3004, https://doi.org/10.1021/acsenergylett.0c01628.

23. N. C. Rosero-Navarro, K. Tadanaga, and A. Miura, "Composite Cathode Prepared by Argyrodite Precursor Solution Assisted by Dispersant Agents for Bulk-type all-Solid-State Batteries," *Journal of Power Sources* 396 (2018): 33–40, https://doi.org/10.1016/j.jpowsour.2018.06.011.

24. I. Kochetkov, T.-T. Zuo, R. Ruess, et al., "Different Interfacial Reactivity of Lithium Metal Chloride Electrolytes with High Voltage Cathodes Determines Solid-state Battery Performance," *Energy & Environmental Science* 15 (2022): 3933–3944, https://doi.org/10.1039/D2EE00803C.

25. S. Wang, J. Liang, S. Li, et al., "Solvent Stability of Halide Solid Electrolytes towards Wet Processing," *Energy Storage Materials* 72 (2024): 103726, https://doi.org/10.1016/j.ensm.2024.103726.

26. Z. Liu, W. Hou, H. Tian, et al., "An Ultralow-Concentration and Moisture-Resistant Electrolyte of Lithium Difluoro(oxalato)Borate in Carbonate Solvents for Stable Cycling in Practical Lithium-Ion Batteries," *Angewandte Chemie International Edition* 63 (2024): 202400110, https://doi.org/10.1002/anie.202400110.

27. B. Jiang, J. Li, B. Luo, et al., "$LiPO_2F_2$ Electrolyte Additive for High-Performance Li-Rich Cathode Material," *Journal of Energy Chemistry* 60 (2021): 564–571, https://doi.org/10.1016/j.jechem.2021.01.024.

28. K. Lee, S. Kim, J. Park, et al., "Selection of Binder and Solvent for Solution-Processed all-Solid-State Batteries," *Journal of the Electrochemical Society* 164 (2017): A2075–A2081.

29. B. Emley, C. Wu, L. Zhao, et al., "Impact of Fabrication Methods on Binder Distribution and Charge Transport in Composite Cathodes of all-Solid-State Batteries," *Materials Futures* 2 (2023): 045102, https://doi.org/10.1088/2752-5724/acefe6.

30. J. Zhang, M. Wu, Z. Zhang, N. Li, C. Tian, and W. Xue, "Sparingly Solvating Electrolyte with Hofmeister Selectivity for Practical Long-Lived Li–Se Batteries," *Angewandte Chemie International Edition* 64 (2025): 11223, https://doi.org/10.1002/anie.202511223.

31. G. Yan, X. Li, Z. Wang, et al., "Fluorinated Solvents for High-voltage Electrolyte in Lithium-Ion Battery," *Journal of Solid State Electrochemistry* 21 (2017): 1589–1597, https://doi.org/10.1007/s10008-017-3508-4.

32. S. Ge, R. S. Longchamps, T. Liu, J. Liao, Y. Leng, and C.-Y. Wang, "High Safety and Cycling Stability of Ultrahigh Energy Lithium Ion Batteries," *Cell Reports Physical Science* 2 (2021): 100584.

33. Z. Cheng, L. Guo, Q. Dong, et al., "Highly Durable and Ultrafast Cycling of Dual-Ion Batteries via in Situ Construction of

Cathode–Electrolyte Interphase," *Advanced Energy Materials* 12 (2022): 2202253, https://doi.org/10.1002/aenm.202202253.

34. B. Deng, H. Wang, X. Li, et al., "Effects of Charge Cutoff Potential on an Electrolyte Additive for $LiNi_{0.6}$ $Co_{0.2}$ $Mn_{0.2}$ O_2 –Mesocarbon Microbead Full Cells," *Energy Technology* 7 (2019): 1800981, https://doi.org/10.1002/ente.201800981.

35. Q. Yu, Z. Chen, L. Xing, et al., "Enhanced High Voltage Performances of Layered Lithium Nickel Cobalt Manganese Oxide Cathode by Using Trimethylboroxine as Electrolyte Additive," *Electrochimica Acta* 176 (2015): 919–925, https://doi.org/10.1016/j.electacta.2015.07.058.

36. B. Tong, Z. Song, H. Wan, et al., "Sulfur-Containing Compounds as Electrolyte Additives for Lithium-Ion Batteries," *InfoMat* 3 (2021): 1364–1392.

37. Q. Sun, Z. Cao, Z. Ma, et al., "Dipole–Dipole Interaction Induced Electrolyte Interfacial Model To Stabilize Antimony Anode for High-Safety Lithium-Ion Batteries," *ACS Energy Letters* 7 (2022): 3545–3556, https://doi.org/10.1021/acsenergylett.2c01408.

38. Z. Guo, Z. Cui, R. Sim, and A. Manthiram, "Localized High-Concentration Electrolytes with Low-Cost Diluents Compatible with both Cobalt-Free $LiNiO_2$ Cathode and Lithium-Metal Anode," *Small* 19 (2023): 2305055, https://doi.org/10.1002/smll.202305055.

39. Y. Chen, Q. He, Y. Zhao, et al., "Breaking Solvation Dominance of Ethylene Carbonate via Molecular Charge Engineering Enables Lower Temperature Battery," *Nature Communications* 14 (2023): 8326, https://doi.org/10.1038/s41467-023-43163-9.

40. A. S. M. C. Rodrigues, A. M. Fernandes, J. Dévemy, M. C. Gomes, and L. M. N. B. F. Santos, "Fluorination Effect in the Volatility of Imidazolium-based Ionic Liquids," *Journal of Molecular Liquids* 282 (2019): 385–391, https://doi.org/10.1016/j.molliq.2019.03.024.

41. S. Li, W. Zhang, Q. Wu, et al., "Synergistic Dual-Additive Electrolyte Enables Practical Lithium-Metal Batteries," *Angewandte Chemie* 132 (2020): 15045–15051, https://doi.org/10.1002/ange.202004853.

42. X. Fan, X. Ji, L. Chen, et al., "All-Temperature Batteries Enabled by Fluorinated Electrolytes with Non-Polar Solvents," *Nature Energy* 4 (2019): 882–890, https://doi.org/10.1038/s41560-019-0474-3.

43. Y.-T. Chen, J. Jang, J. A. S. Oh, et al., "Enabling Uniform and Accurate Control of Cycling Pressure for all-Solid-State Batteries," *Advanced Energy Materials* 14 (2024): 2304327, https://doi.org/10.1002/aenm.202304327.

44. D. Lee, Y. Shim, Y. Kim, et al., "Shear Force Effect of the Dry Process on Cathode Contact Coverage in all-Solid-State Batteries," *Nature Communications* 15 (2024): 4763, https://doi.org/10.1038/s41467-024-49183-3.

45. G. Conforto, R. Ruess, D. Schröder, et al., "Editors' Choice—Quantification of the Impact of Chemo-Mechanical Degradation on the Performance and Cycling Stability of NCM-Based Cathodes in Solid-State Li-Ion Batteries," *Journal of The Electrochemical Society* 168 (2021): 070546, https://doi.org/10.1149/1945-7111/ac13d2.

46. E. P. Alsaç, D. L. Nelson, S. G. Yoon, et al., "Characterizing Electrode Materials and Interfaces in Solid-State Batteries," *Chemical Reviews* 125 (2025): 2009–2119.

47. W. Xie, P. Guo, and X. Gao, "Elucidating the Rate Limitation of Lithium-Ion Batteries under Different Charging Conditions through Polarization Analysis," *Journal of Energy Storage* 82 (2024): 110554, https://doi.org/10.1016/j.est.2024.110554.

48. Y. Lu, C.-Z. Zhao, J.-Q. Huang, and Q. Zhang, "The Timescale Identification Decoupling Complicated Kinetic Processes in Lithium Batteries," *Joule* 6 (2022): 1172–1198, https://doi.org/10.1016/j.joule.2022.05.005.

49. S. Sun, C. Zhao, G. Liu, et al., "Boosting Anionic Redox Reactions of Li-Rich Cathodes through Lattice Oxygen and Li-Ion Kinetics Modulation in Working all-Solid-State Batteries," *Advanced Materials* 37 (2025): 202414195.

50. Y. Li, Q. Qu, L. Lv, J. Shao, and H. Zheng, "A Multifunctional Additive Capable of Electrolyte Stabilization and Structure/Interphases Regulation of High-Energy Li-Ion Batteries," *Advanced Functional Materials* 34 (2024): 2314100, https://doi.org/10.1002/adfm.202314100.

51. J. Li, W. Li, Y. You, and A. Manthiram, "Extending the Service Life of High-Ni Layered Oxides by Tuning the Electrode–Electrolyte Interphase with a Lithium Bis(oxalate)Borate Additive," *Advanced Energy Materials* 8 (2018): 1801957.

52. J. Mao, J. Iocozzia, J. Huang, K. Meng, Y. Lai, and Z. Lin, "Graphene Aerogels for Efficient Energy Storage and Conversion," *Energy & Environmental Science* 11 (2018): 772–799, https://doi.org/10.1039/C7EE03031B.

53. J. Liu, J. Wang, Y. Ni, et al., "Tuning Interphase Chemistry to Stabilize High-Voltage $LiCoO_2$ Cathode Material via Spinel Coating," *Angewandte Chemie International Edition* 61 (2022): 202207000, https://doi.org/10.1002/anie.202207000.

54. J. Tan, J. Matz, P. Dong, J. Shen, and M. Ye, "A Growing Appreciation for the Role of LiF in the Solid Electrolyte Interphase," *Advanced Energy Materials* 11 (2021): 2100046.

55. Y. Qiao, H. Yang, Z. Chang, H. Deng, X. Li, and H. Zhou, "A High-Energy-Density and Long-Life Initial-Anode-Free Lithium Battery Enabled by a Li_2O Sacrificial Agent," *Nature Energy* 6 (2021): 653–662, https://doi.org/10.1038/s41560-021-00839-0.

56. G. Lu, Q. Qiao, M. Zhang, et al., "High-Voltage Electrosynthesis of Organic-Inorganic Hybrid with Ultrahigh Fluorine Content toward Fast Li-Ion Transport," *Science Advances* 10 (2024): ado7348, https://doi.org/10.1126/sciadv.ado7348.

57. S. Perez-Beltran, D. Kuai, and P. B. Balbuena, "SEI Formation and Lithium-Ion Electrodeposition Dynamics in Lithium Metal Batteries via First-Principles Kinetic Monte Carlo Modeling," *ACS Energy Letters* 9 (2024): 5268–5278, https://doi.org/10.1021/acsenergylett.4c02019.

58. X. Xiong, T. Lin, C. Tian, et al., "Creep-type All-Solid-State Cathode Achieving Long Life," *Nature Communications* 15 (2024): 3706, https://doi.org/10.1038/s41467-024-48174-8.

59. L. Shen, J. Li, W. Kong, et al., "Anion-Engineering toward High-Voltage-Stable Halide Superionic Conductors for all-Solid-State Lithium Batteries," *Advanced Functional Materials* 34 (2024): 2408571, https://doi.org/10.1002/adfm.202408571.

60. L. Britala, M. Marinaro, and G. Kucinskis, "A Review of the Degradation Mechanisms of NCM Cathodes and Corresponding Mitigation Strategies," *Journal of Energy Storage* 73 (2023): 108875, https://doi.org/10.1016/j.est.2023.108875.

61. J. Wandt, A. T. S. Freiberg, A. Ogrodnik, and H. A. Gasteiger, "Singlet Oxygen Evolution from Layered Transition Metal Oxide Cathode Materials and Its Implications for Lithium-ion Batteries," *Materials Today* 21 (2018): 825–833, https://doi.org/10.1016/j.mattod.2018.03.037.

62. B. L. D. Rinkel, J. P. Vivek, N. Garcia-Araez, and C. P. Grey, "Two Electrolyte Decomposition Pathways at Nickel-rich Cathode Surfaces in Lithium-ion Batteries," *Energy & Environmental Science* 15 (2022): 3416–3438, https://doi.org/10.1039/D1EE04053G.

63. W. Kim, J. Noh, S. Lee, et al., "Aging Property of Halide Solid Electrolyte at the Cathode Interface," *Advanced Materials* 35 (2023): 2301631, https://doi.org/10.1002/adma.202301631.

64. M. Fan, X. Meng, H. Guo, et al., "Reviving Fatigue Surface for Solid-State Upcycling of Highly Degraded Polycrystalline $LiNi_{1-X-y}$ Co_X Mn_y O_2 Cathodes," *Advanced Materials* 36 (2024): 2405238, https://doi.org/10.1002/adma.202405238.

65. L. Zou, W. Zhao, H. Jia, et al., "The Role of Secondary Particle Structures in Surface Phase Transitions of Ni-Rich Cathodes," *Chemistry of Materials* 32 (2020): 2884–2892, https://doi.org/10.1021/acs.chemmater.9b04938.

66. S. Yin, W. Deng, J. Chen, et al., "Fundamental and Solutions of Microcrack in Ni-Rich Layered Oxide Cathode Materials of

Lithium-Ion Batteries," *Nano Energy* 83 (2021): 105854, https://doi.org/10.1016/j.nanoen.2021.105854.

67. E. D. Orlova, A. A. Savina, S. A. Abakumov, A. V. Morozov, and A. M. Abakumov, "Comprehensive Study of Li^{+}/Ni^{2+} Disorder in Ni-Rich NMCs Cathodes for Li-Ion Batteries," *Symmetry* 13 (2021): 1628.

68. Z. Yang, Z. Zhao, X. Zhang, et al., "Sb-Anchoring Single-Crystal Engineering Enables Ultra-High-Ni Layered Oxides with High-Voltage Tolerance and Long-Cycle Stability," *Nano Energy* 132 (2024): 110413, https://doi.org/10.1016/j.nanoen.2024.110413.

69. H. Chen, H. Yuan, Z. Dai, et al., "Surface Gradient Ni-Rich Cathode for Li-Ion Batteries," *Advanced Materials* 36 (2024): 2401052, https://doi.org/10.1002/adma.202401052.

Supporting Information

Additional supporting information can be found online in the Supporting Information section.

Supporting File: aenm70963-sup-0001-SuppMat.docx.